

# Near-infrared integral field spectroscopy of Massive Young Stellar Objects

K. Murakawa<sup>1</sup>, S. L. Lumsden<sup>1</sup>, R. D. Oudmaijer<sup>1</sup>, B. Davies<sup>2</sup>,  
H. E. Wheelwright<sup>3</sup>, M. G. Hoare<sup>1</sup>, and J. D. Ilee<sup>1,4</sup>

<sup>1</sup>*School of Physics and Astronomy, EC Stoner Building, University of Leeds, Leeds LS2 9JT*

<sup>2</sup>*Institute of Astronomy, University of Cambridge, Madingley Road, Cambridge CB3 0HA*

<sup>3</sup>*Max-Planck-Institut für Radioastronomie, Auf dem Hügel 69, 53121, Bonn, Germany*

<sup>4</sup>*School of Physics and Astronomy, University of St Andrews, St Andrews KY16 9SS*

Accepted 1988 December 15. Received 1988 December 14; in original form 1988 October 11

## ABSTRACT

We present medium resolution ( $R \approx 5300$ )  $K$ -band integral field spectroscopy of six massive young stellar objects (MYSOs). The targets are selected from the Red MSX Source (RMS) survey, and we used the ALTAIR adaptive optics assisted Near-Infrared Integral Field Spectrometer (NIFS) mounted on the Gemini North telescope. The data show various spectral line features including  $\text{Br}\gamma$ , CO,  $\text{H}_2$ , and He I. The  $\text{Br}\gamma$  line is detected in emission in all objects with  $v_{\text{FWHM}} \sim 100 - 200 \text{ km s}^{-1}$ . V645 Cyg shows a high-velocity P-Cygni profile between  $-800 \text{ km s}^{-1}$  and  $-300 \text{ km s}^{-1}$ . We performed three-dimensional spectroastrometry to diagnose the circumstellar environment in the vicinity of the central stars using the  $\text{Br}\gamma$  line. We measured the centroids of the velocity components with sub-mas precision. The centroids allow us to discriminate the blueshifted and redshifted components in a roughly east–west direction in both IRAS 18151–1208 and S106 in  $\text{Br}\gamma$ . This lies almost perpendicular to observed larger scale outflows. We conclude, given the widths of the lines and the orientation of the spectroastrometric signature, that our results trace a disc wind in both IRAS 18151–1208 and S106. The CO  $\nu = 2 - 0$  absorption lines at low  $J$  transitions are detected in IRAS 18151–1208 and AFGL 2136. We analysed the velocity structure of the neutral gas discs, which we find to have nearly Keplerian motions. In IRAS 18151–1208, the absorption centroids of the blueshifted and redshifted components are separated in a direction of north-east to south-west, nearly perpendicular to that of the larger scale  $\text{H}_2$  jet. The position-velocity relations of these objects can be reproduced with central masses of  $30 M_{\odot}$  for IRAS 18151–1208 and  $20 M_{\odot}$  for AFGL 2136. We also detect CO  $\nu = 2 - 0$  bandhead emission in IRAS 18151–1208, S106 and V645 Cyg. The results can be fitted reasonably with a Keplerian rotation model, with masses of 15, 20 and  $20 M_{\odot}$  respectively. These results for a sample of MYSOs can be explained with disc and outflow models and support the hypothesis of massive star formation via mass accretion through discs as is the case for lower mass counterparts.

**Key words:** ISM: H II region – ISM: individual: IRAS 18151–1208, AFGL 2136, IRAS 19065+0526, S106 IRS4, G082.5682+00.4040, and V645 Cyg.

## 1 INTRODUCTION

The formation of high-mass stars ( $M_{\star} \geq 8M_{\odot}$ ) is one of the fundamental issues in astrophysics. The formation mechanism of low-mass stars via accretion through a circumstellar disc is generally believed to be well understood (e.g. Shu et al. 1987). However, it was realised relatively early that the same mechanism for massive star formation poten-

tially suffered from problems due to the immense radiation pressure from the forming star (e.g. Khan 1974). High-mass stars are usually expected to have short Kelvin-Helmholtz time scales ( $\leq 10^4 \text{ yr}$ ), so that nuclear burning begins while the gaseous material is still accreting from the natal cloud, and before the star exceeds  $\sim 10 M_{\odot}$  (Shu et al. 1987). The resultant radiation pressure from that burning acts on both

**Table 1.** Physical parameters of the target objects

target		position <sup>1</sup> (J=2000)		$L_{\star}^1$	$M_{\star}^2$	spc. type	$D^1$	brightness <sup>1</sup>
	RMS name	R.A.	Dec.	$L_{\odot}$	$M_{\odot}$		kpc	$m_K$
IRAS 18151–1208	G018.3412+01.7681	18 17 58.1	−12 07 24.8	$2.2 \times 10^4$	15	B0 <sup>3</sup>	2.8	9.3
AFGL 2136	G017.6380+00.1566	18 22 26.4	−13 30 12.0	$5.3 \times 10^4$			2.2	7.3
IRAS 19065+0529	G039.9018−01.3513	19 09 02.5	+05 34 42.2	$1.0 \times 10^4$			3.2	11.6
S106 IRS4	G076.3829−00.6210	20 27 26.8	+37 22 47.7	$4.0 \times 10^4$	20	O9Ve–B0Ve <sup>4</sup>	1.4	5.9
G082.5682+00.4040	G082.5682+00.4040a	20 42 33.7	+42 56 51.3	$4.2 \times 10^3$			1.4	9.7
V645 Cyg	G094.6028−01.7966	21 39 58.3	+50 14 20.9	$4.3 \times 10^4$	20	O7e <sup>5</sup>	4.9	6.8

<sup>1</sup> The values are from the RMS data base. <sup>2</sup> Rough estimation from the spectral types. <sup>3</sup> Fallscheer et al. (2011), and Appendix A. <sup>4</sup> Hanson, Conti & Rieke (1996). <sup>5</sup> Cohen et al. (1977).

the gas and dust surrounding the star, counteracting further accretion (e.g. Zinnecker & Yorke 2007). This eventually led to the discussion of models in which massive stars formed through much more dynamical processes, such as competitive accretion (e.g. Bonnell et al. 2004). However an alternative mechanism exists which preserves the connection with low mass star formation. The high densities and degree of turbulence and short timescales involved in high mass star formation regions lead to accretion rates sufficient to ensure the infalling material can overcome the radiation pressure (e.g. McKee & Tan 2003). In addition, the role of outflows in creating channels for the radiation to escape, reducing the pressure in the circumstellar environment, had also been underestimated (e.g. Yorke & Sonnhalter 2002).

Recent, more detailed, numerical calculations have shown that the conclusions of McKee & Tan and Yorke & Sonnhalter are substantially correct, at least in showing that massive stars can form in such an environment. The collimated outflows do help to reduce the radiation pressure, but also act to generate further turbulence in the surrounding molecular cloud, effectively helping sustain the conditions required by the McKee & Tan model. Models by Krumholz et al. (2009, 2010), using an approximate treatment of the radiation field, found that the role of the disc and outflow cavity was crucial. Kuiper et al. (2010) have shown that a full radiative transfer treatment results in there being essentially no limit to the mass of star that can be formed, since the disc effectively self-shields against the star’s radiation pressure. More recently Kuiper & Yorke (2013) have shown that gas, rather than dust, opacity above the disc creates an additional shield, so that the “radiation pressure” problem is reduced even further.

Direct detection of small scale discs around young massive protostars is however observationally challenging (e.g. Kraus et al. 2010). We have pioneered the use of spatially resolved near-infrared spectroscopy in this field to help address the issue of the properties of discs around massive protostars, as well as any small scale outflows present (e.g. Davies et al. 2010), and this paper follows on from our earlier work.

The near-infrared (NIR) spectra of massive young stellar objects (MYSOs) show a variety of important diagnostic emission and absorption features. For example, hydrogen recombination lines such as Br $\gamma$  (H I  $n = 7 - 4$  at  $2.166 \mu\text{m}$ ) are emitted from ionized regions. They are often used as tracers of the mass accretion in lower mass stars (e.g.

Greene & Lada 1996; Najita et al. 1996; Muzerolle et al. 1998; Folha & Emerson 2001), as well as of stellar and disc winds (e.g. Persson 1984; Bunn et al. 1995; Nisini et al. 1995; Corcoran & Ray 1998; Drew et al. 1998; Ishii et al. 2001) at all masses. The former show low velocity ( $|v| \lesssim 100 - 200 \text{ km s}^{-1}$ ) emission, often with associated weak red absorption features from the infalling gas, while the latter show wider velocity ranges ( $v \lesssim 200 - 600 \text{ km s}^{-1}$ ) and sometimes a P-Cygni absorption profile suggesting an outflowing wind (e.g. Drew et al. 1998; Kurosawa et al. 2011; Lumsden et al. 2012). Another interesting feature is the first overtone rovibrational spectrum of carbon monoxide around  $2.3 \mu\text{m}$ . The CO bandhead is often seen in emission and is thought to arise from accretion discs of neutral gas with temperatures ranging between  $\sim 2000 \text{ K}$  and  $\sim 5000 \text{ K}$ . These features are therefore useful in tracing structures ranging from the hot ionized gas to a warm dusty disc. If the gaseous CO discs show Keplerian rotation at a radius of  $0.1 \text{ AU}$ , and the mass of the central star is  $\sim 10 M_{\odot}$ , the rotation velocity is  $\sim 300 \text{ km s}^{-1}$ , which can be analysed by medium and high resolution spectroscopy. In fact, the observed CO  $\nu = 2 - 0$  bandhead emission in young stellar objects as a whole can be explained with Keplerian rotating disc models (e.g. Black & Willner 1984; Carr 1989; Chandler et al. 1995; Najita et al. 1996; Martin 1997; Kraus et al. 2000; Bik & Thi 2004; Wheelwright et al. 2010).

Recently, some results of NIR integral field spectroscopy using 8 m class telescopes have been reported (Davies et al. 2010; Goto et al. 2012; Stecklum et al. 2012). With this method, we obtain the images and spectra simultaneously and can perform spectro-astrometry. The technique allows us to measure the position centroids of the circumstellar features with sub-mas accuracy. Using 3D spectro-astrometry, Davies et al. (2010, hereafter D10) showed that the Br $\gamma$  emission line in the MYSO W33A reveals evidence for a fast bipolar jet ( $v \sim 600 \text{ km s}^{-1}$ ) on sub-milliarcsec scales (cf. the intrinsic angular resolution of an 8m telescope of  $\sim 100 \text{ mas}$  in the  $K$  band). From a velocity analysis of the CO  $\nu = 2 - 0$  bandhead, they estimated the stellar mass to be  $10 - 15 M_{\odot}$ . We have extended the same technique as used by D10 to a sample of MYSOs selected from the RMS (Red MSX Source survey, Lumsden et al. 2002) and search for the aforementioned signatures. Sect. 2.1, describes the observations and the data reduction procedure, and presents the images and spectra. We perform the analysis of the Br $\gamma$  emission lines and the velocity structures from the CO spectra of selected

**Table 2.** NIFS integral field spectroscopy observations

target	int. time	standard		date
	sec	ID	spc. type	
I18151	2880	HR 6956	A5IV	2011-07-17
AFGL 2136	900	HR 7288	A3V	2011-07-15
I19065	1440	HR 8291	A2V	2011-07-15
S106	510	HR 7734	A0V	2011-07-14
G082	1080	HR 7752	A1V	2011-07-13
V645 Cyg	200	HR 8291	A2V	2011-07-19

targets in Sect. 4. Appendix A provides a discussion of individual objects.

## 2 NIFS INTEGRATED FIELD SPECTROSCOPY

### 2.1 Observations

We observed six MYSOs using the Gemini Near-Infrared Integral Field Spectrograph (NIFS; McGregor et al. 2003) on the nights between 2011 July 13 and July 19. The target objects are IRAS 18151–1208 (hereafter I18151), AFGL 2136, IRAS 19065+0529 (hereafter I19065), S106 IRS4 (hereafter S106), G082.5682+00.4040 (hereafter G082), and V645 Cyg, which were selected from the RMS catalogue (Lumsden et al. 2013). These, together with W33A from BD10, form a complete set of objects for which the central star was sufficiently bright for infrared spectroscopy, but also, more crucially, where a bright optical guide star was present within 20 arcseconds of the target. They are a rather heterogeneous collection of objects in other regards. I19065 is listed as a weak compact HII region in the RMS catalogue, S106 has elements of both a massive protostar and an HII region. In both cases we centred the NIFS aperture on the apparent exciting star. The basic properties of all sources (distance, luminosity, apparent  $K$  band magnitude) are listed in Table 2. A summary of the known properties of these objects and how these tie in with the current observations can be found in the Appendix.

The instrument acquires a  $3 \times 3$  arcsec<sup>2</sup> field of view which is separated into 29 slices and is recorded on a two-dimensional infrared detector with  $2048 \times 2048$  pixels. The  $K$ -band spectrum with a wavelength range between 2.0 and 2.4  $\mu\text{m}$  is obtained, with a spectral resolution of  $R \approx 5500$  corresponding to a velocity resolution of  $\approx 55 \text{ km s}^{-1}$ . The ALTAIR adaptive optics system was used to correct the wavefront of the target object for all sources except S106, for which no suitable guide star was available. The system uses a natural-guide star for tip-tilt correction and the laser-guide star for wavefront sensing.

In our observations, the target objects and the sky field were observed in turns. The offset of the sky field is between 20 arcsec and 30 arcsec. In addition to the science targets, we observed standard stars to correct for telluric absorption lines. The Gemini facility calibration plan was used. This includes the dark frames, the flat field data, Argon-Xenon (Ar-Xe) arc lamp for wavelength calibration, and Ronchi

screen images to calibrate the spatial distortion of the NIFS data. The observing log is provided in Table 2.

### 2.2 Data reduction

Dark frames and flat field frames were constructed for each observation date. High ADU counts in the dark frames and low counts in the flat field frames are assumed to be due to hot and dead pixels, respectively. Bad pixel frames that include this information were created.

The preprocessing, the dark frame subtraction, flat fielding, and removal of bad pixels were performed for the targets, standards, arc lamp, and Ronchi frames. In the next step, the Ar-Xe lamp data were used for wavelength calibration, the Ronchi screen data were used to correct the image distortion, and the two-dimensional images were converted into three-dimensional ( $x, y, \lambda$ ) cubes. In the data before this conversion, the pixel scales are 0.043 arcsec in the space axis in each slice and 0.103 arcsec of the position increment of the neighbouring slice. Each wavelength element (2 pixels) has  $\Delta\lambda \approx 0.00041 \mu\text{m}$  which equates to a velocity width of  $\approx 56 \text{ km s}^{-1}$ .

The sky frames were then subtracted from the target frames and the correction for the telluric absorption features was made. The telluric standard stars have spectral types around A0V, in which the metal lines are relatively weak and infrequent (Vacca et al. 2003). The standard stars show a strong, intrinsic Br $\gamma$  absorption line, which needs to be removed from the standard star data before they can be used to correct for the telluric absorption in the targets. For this purpose, the Br $\gamma$  absorption line was fitted using the `de-blend` command of the `onedspec` task of the IRAF data reduction software and the modeled function was removed from the standard star spectrum. The target data were then divided by the corrected standard star data and were multiplied with a blackbody function with an effective temperature corresponding to their spectral type.

The angular resolution was determined by measuring the full width at half maximum of the telluric standards, which are single stars. The typical values are  $\sim 0.1$  arcsec, which are constant through the entire wavelength range.

For the one-dimensional spectra, where all the fluxes at individual wavelength channels are integrated through the ( $x, y$ ) space, the typical SNRs are found to be 100 – 300 per wavelength channel. The spectral resolution is measured from unresolved telluric absorption lines in the telluric standard stars. The typical values are  $\sim 0.00037 \mu\text{m}$  ( $\Delta v \sim 48 \text{ km s}^{-1}$ ). We also measured the statistical variations of the wavelengths of the telluric absorption features of the standard stars. By comparing with the wavelength channel positions of these features of stars that were observed at different times and dates, we obtained an error of  $\sim 10^{-5} \mu\text{m}$  ( $\sim 1.3 \text{ km s}^{-1}$ ), which is about one tenth of one wavelength channel.

I19065 and V645 Cyg were also observed on 2011 July 17 and 15, respectively, in addition to the dates that are indicated in Table 2. The integration times of the targets are 1980 sec. for I19065 and 700 sec. for V645 Cyg. For I19065, the SNR of the spectrum is  $\sim 100$ , which is worse than that of the data taken on July 15 ( $\sim 140$ ). This is due to non-photometric conditions at the time of observing I19065 on July 17. This leads to very poor subtraction of the night sky

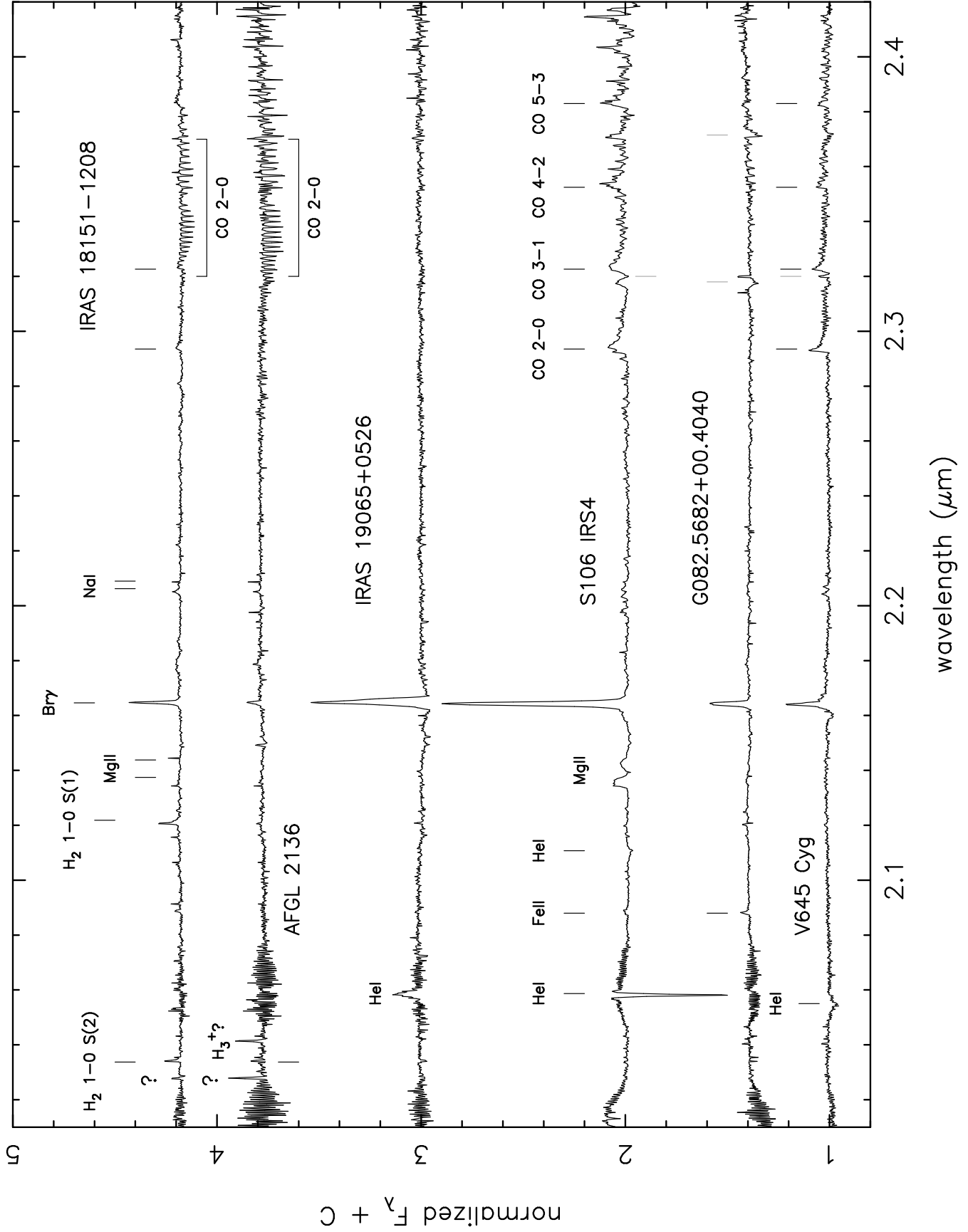


**Figure 1.** *K*-band spectra of our target objects obtained using the Gemini-north/NIFS instrument.

**Table 3.** Identified emission and absorption lines in our observations

target	Br $\gamma$	CO	others
	$v_{\text{LSR}}^1/v_{\text{FWHM}}/v_{\text{FWZI}}$	$2.3 \mu\text{m}^3$	
I18151	34.2(32.8)/108/ $\pm 158$	$\nu = 2 - 0^4, 3 - 1$	H <sub>2</sub> 1-0 S(1), S(2), Mg II, Na I
AFGL 2136	21.4(22.5)/133/ $\pm 114$	$\nu = 2 - 0^4$	H <sub>2</sub> 1-0 S(1), S(2), Na I
I19065	18.0(12.5)/211/ $\pm 258$	no	He I
S106	8.09(-1.7)/190/ $\pm 220$	$\nu = 2 - 0, 3 - 1, 4 - 2, 5 - 3$	He I, Fe II
G082	-2.87(-4.1)/215/ $\pm 230$	no	Fe II
V645 Cyg	-44.4(-43.9)/157/ $\pm 396^2$	$\nu = 2 - 0, 3 - 1, 4 - 2, 5 - 3$	He I

<sup>1</sup> The values in the parenthesis are from the RMS data base. <sup>2</sup> Since the feature shows a P Cyg profile, the value is provided only for the redder side. <sup>3</sup> Vacuum wavelengths of the bandhead are  $2.29353 \mu\text{m}$  for  $\nu = 2 - 0$ ,  $2.32265 \mu\text{m}$  for  $\nu = 3 - 1$ ,  $2.35246 \mu\text{m}$  for  $\nu = 4 - 2$  and  $2.38295 \mu\text{m}$  for  $\nu = 5 - 3$  (Tokunaga 2000). <sup>4</sup> Absorption in the *R* and *P* branches is also detected.

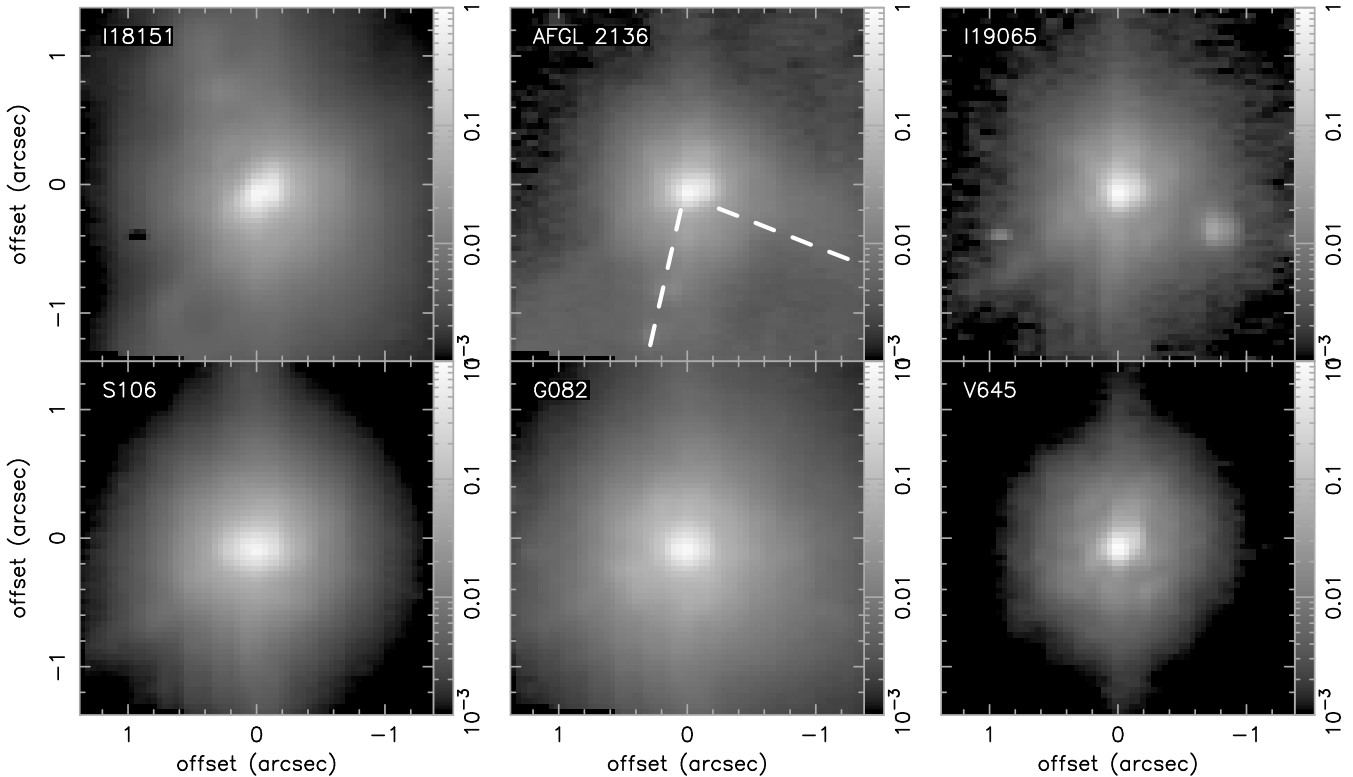


**Figure 2.** *K*-band continuum images of our target objects. North is up and East to the left, except for V645 Cyg, where the image is rotated counterclockwise by  $20^\circ$ . The surface brightness is normalised by the maximum value. In AFGL 2136, the V-shaped feature is indicated with dashed line.

emission lines in the object minus sky pairs. For V645 Cyg, the detector output signal level was saturated, and hence not suitable for spectroastrometry. For the observations of July 19, the exposure time was reduced from 25 seconds to 20 seconds, and a neutral density filter KG3\_ND\_FILTER\_G5619 with a transparency of 5% was inserted to avoid the saturation. The signal-to-noise in the nebula in the data using the filter are lower, but inspection of the unsaturated parts of the image from July 15 shows no additional information is present. We therefore prefer to use only the data from July 19 in this paper for V645 Cyg, and only that from July 15 for I19065.

### 3 RESULTS

Here we describe the spectral lines and images detected in our data, we defer detailed analysis of interesting lines until Sect. 4.

#### 3.1 2.0 to $2.4 \mu\text{m}$ spectra

Figure 1 presents the 2.0 to  $2.4 \mu\text{m}$  spectra of the target objects. To highlight the emission and absorption lines, the spectra are normalised by a fourth-degree polynomial fit to the continuum. Table 3 lists the lines identified in our observations.

In all target objects, the Br $\gamma$  line is detected in emis-

sion. The Br $\gamma$  emission of V645 Cyg shows a P-Cygni profile. I19065 may show weak photospheric absorption. A series of CO emission and absorption features is detected between 2.3 and 2.4  $\mu\text{m}$ . In I18151 and AFGL 2136, the  $R$  and  $P$  branches of  $\nu = 2 - 0$  lines at low  $J$  transitions are in absorption. Bandhead emissions of  $\nu = 2 - 0$ ,  $3 - 1$ ,  $4 - 2$ , and  $5 - 3$  are detected in S106 and V645 Cyg. In I18151,  $\nu = 2 - 0$ ,  $3 - 1$  and  $5 - 3$  are seen – any  $4 - 2$  emission is masked by the CO absorption. In S106, G082, and V645 Cyg, absorption features are detected around 2.32  $\mu\text{m}$  and 2.372  $\mu\text{m}$ , which are indicated with grey lines in Fig. 1. These features vary significantly when other telluric standard spectra are used. Hence, we conclude that these are residual telluric features that were not fully corrected for. Other lines that are identified are the molecular hydrogen lines in I18151 ( $\nu = 1 - 0$  S(1) and S(2)). For He I, absorption (S106 and V645 Cyg) and emission (I19065) lines at 2.05869  $\mu\text{m}$  ( $2^1P - 2^1S$ ) and an absorption line at 2.1127  $\mu\text{m}$  ( $4^{1,3}S - 1,3P$  in S106) are detected. We also identified Mg II in S106, Na I in I18151 and AFGL 2136, and Fe II in S106 and G082. In AFGL 2136, an emission line is seen at 2.041  $\mu\text{m}$ . The  $2\nu_2(\nu_2 = 2 - 0)$  Q(3–0) transition of H $_3^+$  falls at this wavelength but the lack of other transitions in the same range from the overtone suggests this is an unlikely identification.

### 3.2 NIFS images

Figure 2 shows the  $K$ -band continuum images. I18151 exhibits a knot at NNE and a lobe at a distance of (0.63,  $-1.08$ ) in arcsec from the central star IRS 1. When comparing with the images published by (Davis et al. 2004, hereafter D04), at first glance our image looks rotated by  $180^\circ$ , e.g. a lobe is seen at east in their image in their Fig. 6a. However, this is not the case. The ring-like feature in their image is at a distance of about 2 arcsec from the central star, while the feature in our image is at  $\sim 1$  arcsec. Figure 3 shows the H $_2$   $\nu = 1 - 0$  S(1) image. We see a bright lobe at south-east, which corresponds to the lobe in our  $K$ -band continuum image. This feature is actually the SE jet identified by D04 (see their Fig. 6c). We should note that our AO assisted data have a much higher resolution than D04’s images which were obtained using a 4 m telescope under the seeing limit (although the seeing or beam size is not described in their paper). As a result our images show much more detailed structures. In particular, the jet is pointing south nearer to the star.

The AFGL 2136 image reveals a V-shaped feature expanding toward the south-west. In the previous  $K$ -band image obtained using the 8 m Subaru telescope (Murakawa et al. 2008), the central star (IRS 1) feature looks nearly spherical, however their observations were not performed with AO due to the lack of a bright reference, while here we use laser guide stars and as a result achieve a higher resolution. The V-shaped feature is a little puzzling. The southern arm corresponds to the S-lobe(s) (Kastner et al. 1992; Murakawa et al. 2008). However, the western arm was not detected in the previous observation. Although an extended filament feature is detected at south-east in the previous images, identified as SE-lobe (Kastner et al. 1992), this is detached from IRS 1. The CO  $J = 2 - 1$  emission line image shows a pair of blueshifted (14 to 20  $\text{km s}^{-1}$ ) and redshifted (24 to 30  $\text{km s}^{-1}$ ) components, which extend toward south-east and north-west, respectively

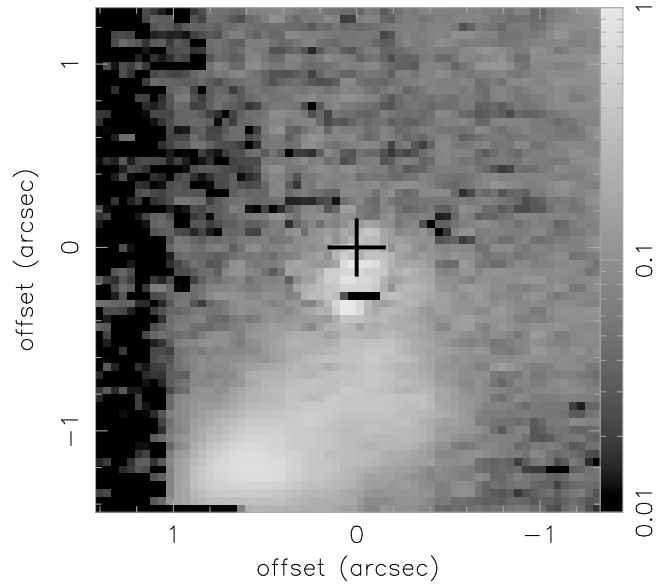


**Figure 3.** H $_2$   $\nu = 1 - 0$  S(1) image of I18151. The cross at the zero-point indicates the position of the flux peak of the  $K$ -band continuum.

(Kastner et al. 1994). The NIR polarimetric images clearly show a centro-symmetric vector pattern surrounding IRS 1 and a polarization disc extending at a position angle of  $\sim 45^\circ$  (Minchin et al. 1991; Kastner et al. 1992; Murakawa et al. 2008). It is reasonable to assume that IRS 1 is the central (proto-)star powering the CO outflow and illuminates the surrounding lobes, which is probably the cavity wall, and the polarization disc is a signature of the presence of an optically thick dust disc/torus. Although it is not conclusive, taking into account these geometrical configurations as well as a detection of a lobe at NNW, the western arm revealed in our image could be the counterpart of the NNW lobe and these two features are the cavity wall of the northern nebulosity.

The other images are point source like. The measured FWHM of the images are  $\sim 0.2$  arcsec apart from V645 Cyg for which it is 0.12 arcsec. S106 IRS4 is a deeply embedded O-type young stellar object that excites the H II region S106 (Sharpless 1959; Sibille et al. 1975; Gehrz et al. 1982; Richer et al. 1993). The previous near-infrared imaging of an arcmin scale field of view have shown a butterfly shaped nebulosity (e.g. Saito et al. 2009). The nebulosity is split by an optically thick dark lane ( $A_V \sim 21$  mag, Felli et al. 1984). It would be reasonable to expect that our image with a small field of view shows the central star feature seen through the dust disc and the scattered light, which causes a slightly extended nebulosity (cf. the PSF FWHM size of the telluric standard star is about 0.1 arcsec). The V645 Cyg star forming region has three optical knots and our target is N0 (Cohen et al. 1977). The previous near-infrared images detected an arc-like feature around the central star (e.g. Cohen et al. 1977; Goodrich 1986; Minchin et al. 1991; Clarke et al. 2006). Because of its characteristic appearance, the nebula is named the “duck nebula” (Goodrich 1986). With improved spatial resolution observations, the appearance does not look like a duck anymore, but the name has stuck. The surface brightness of the central star is signifi-

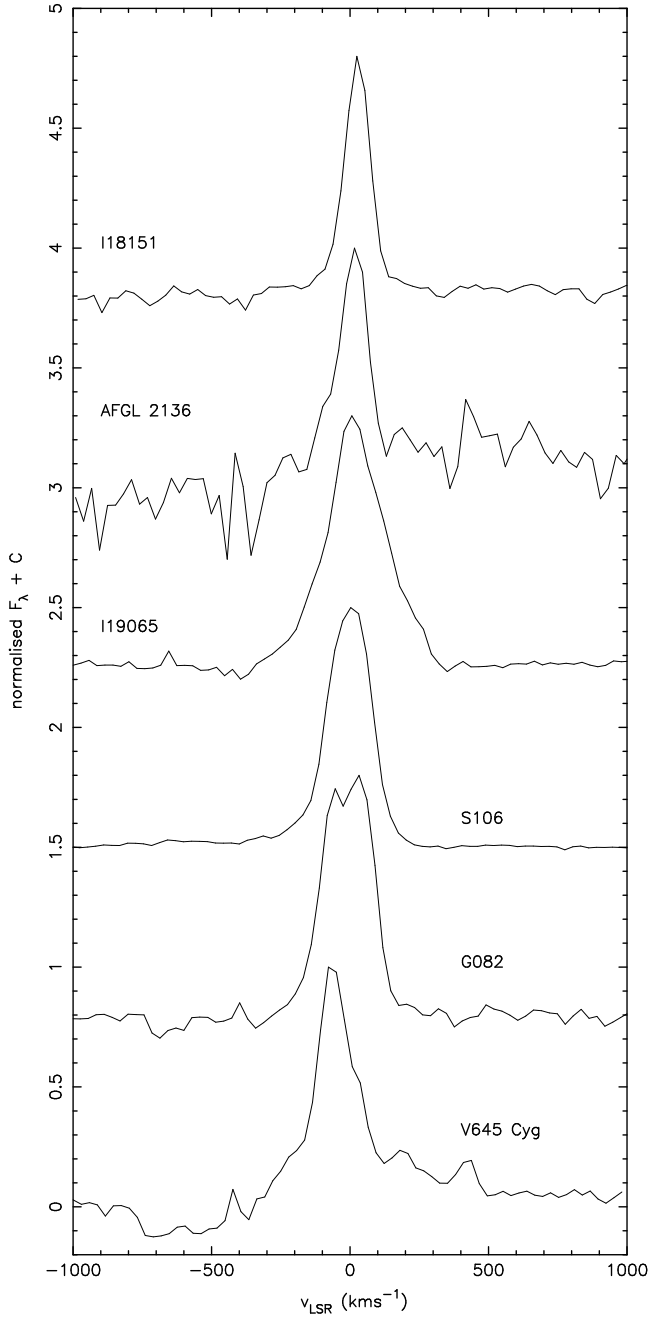


**Figure 4.** The Br $\gamma$  spectral feature on velocity scale.

cantly higher than that of the arc-like feature. This and the FWHM, which is close to that of the standard stars, suggests that the nebulosity is optically thin in the optical and near-infrared.

Several spectral lines are detected in the one-dimensional spectra, as presented in the previous section. The images of these lines look similar to those of the continuum apart from the molecular hydrogen image of I18151. We will constrain our further discussion to the Br $\gamma$  line (Sect. 4.1), the CO  $\nu = 2 - 0$  emission and absorption (Sect. 4.2), and the He I lines (Sect. 4.3).

## 4 SPECTRAL LINE DATA

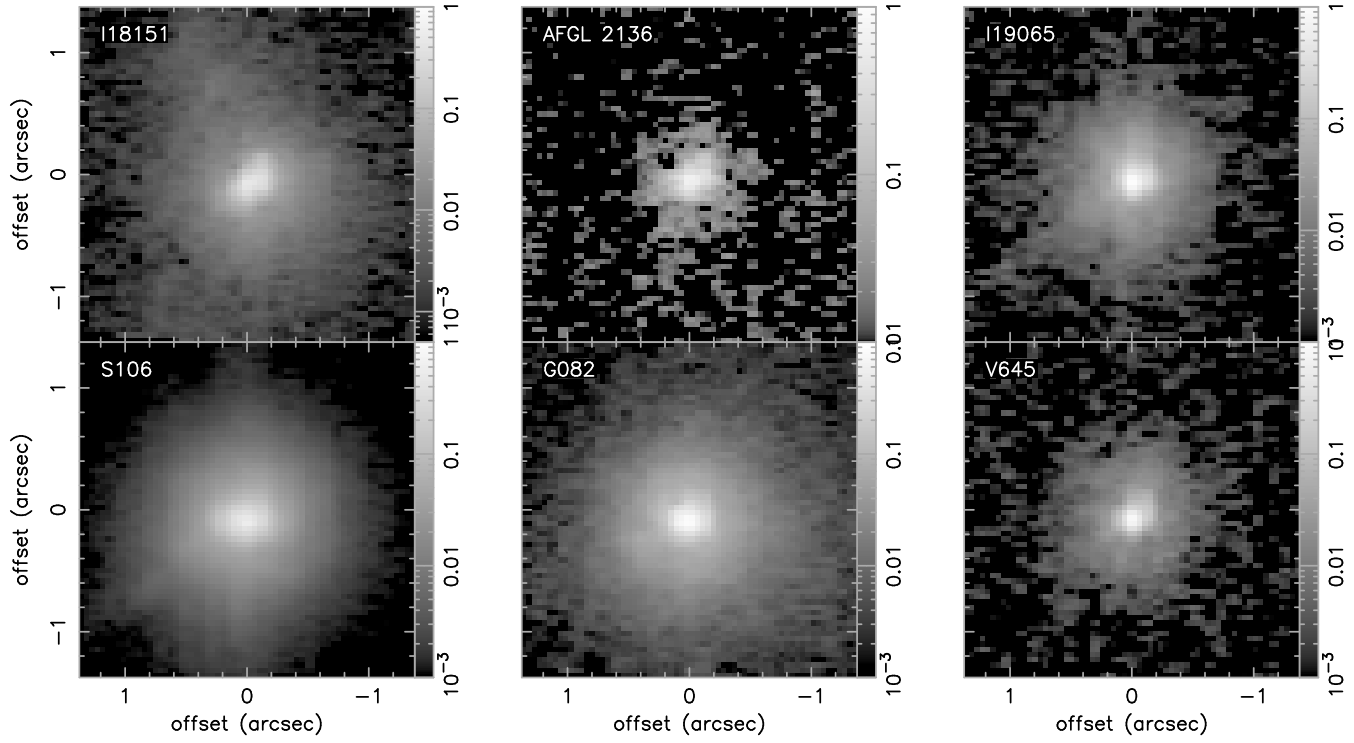
### 4.1 Br $\gamma$ emission

Figure 4 presents the Br $\gamma$  spectra on a  $v_{\text{LSR}}$  scale. The velocities with respect to the local standard of rest,  $v_{\text{LSR}}$ , the full width at half maximum  $v_{\text{FWHM}}$ , and the full width at zero intensity  $v_{\text{FWZI}}$  are listed in Table 3. The  $v_{\text{LSR}}$  values in the parenthesis are from the RMS sources. The discrepancies between the RMS measurements and ours can be explained with the uncertainties of the measured velocity (see Sect. 2.2) with the exception of I19065 and S106. The deviation seen in S106 is relatively small, and the value derived for Br $\gamma$  is consistent with that seen in Lumsden et al. (2012). In I19065, CO  $J = 1 - 0$  emission is detected at two velocities (Urquhart et al. 2007), with  $v_{\text{LSR}}$  of  $+12.5 \text{ km s}^{-1}$  and  $+48.4 \text{ km s}^{-1}$ . The latter of these is coincident with NH $_3$  (1,1) emission, as well as a water maser complex. It is possible that the redder component is from another cloud which is located within the aperture ( $\sim 30 \text{ arcsec}$ ) of the molecular line observations but not within our observations. No other equally bright mid-infrared sources are evident within such an aperture however as seen from the RMS database. The correct molecular line counterpart to the infrared source presented here cannot be resolved with the data currently available however.

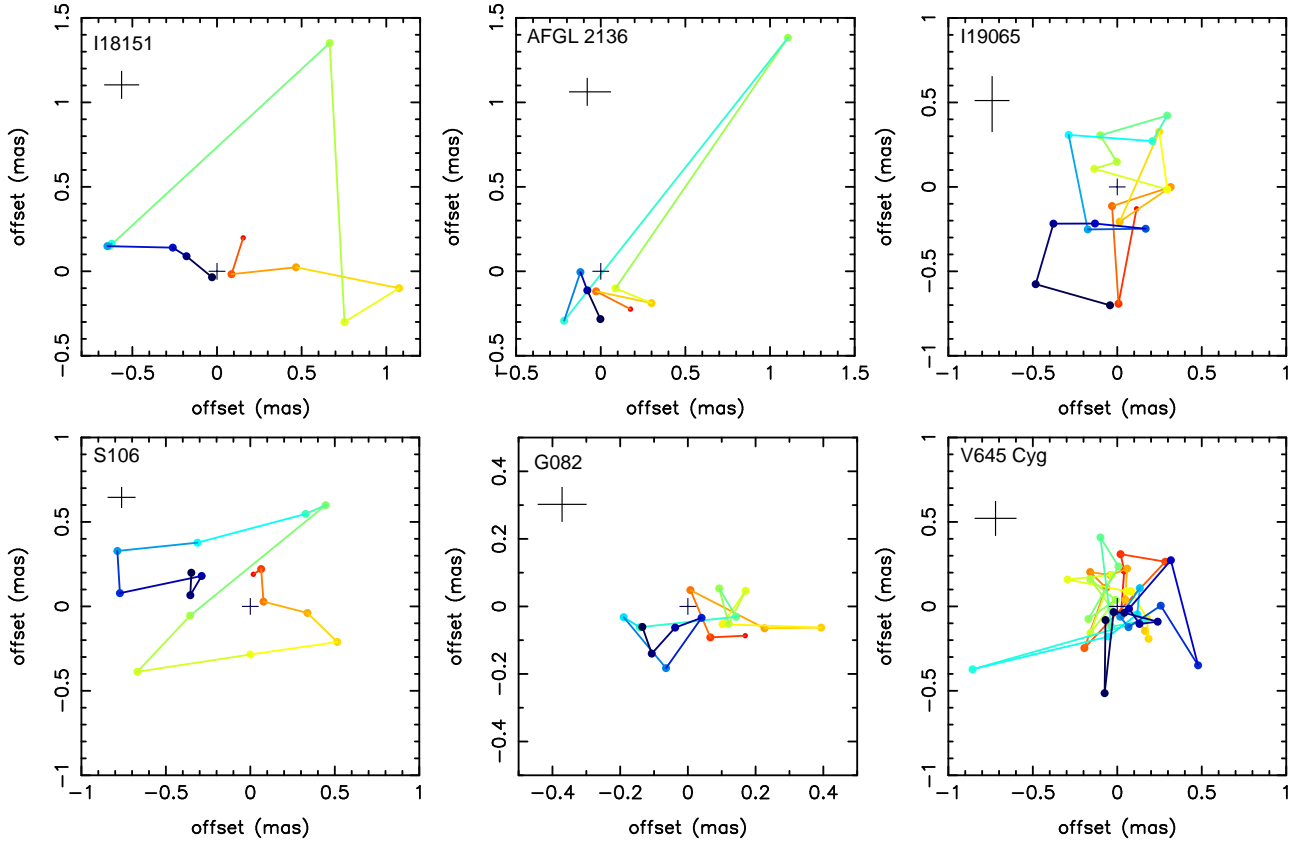
The spectral lines have a bell shape in general, with FWHM ranging from 100 to 220  $\text{km s}^{-1}$ . These values are consistent with the outflow velocities observed by Bunn et al. (1995). In V645 Cyg, we see a P-Cygni profile in the velocity range between  $-800 \text{ km s}^{-1}$  and  $-300 \text{ km s}^{-1}$ . The Br $\gamma$  emission from AFGL 2136 is relatively weak compared to the other sources. The Br $\gamma$  luminosity has a positive correlation with the accretion rate in lower mass stars (Muzerolle et al. 1998; Mendigutia et al. 2011), hence the weak Br $\gamma$  emission may be the result of a low accretion rate (e.g. Folha & Emerson 2001; Antonucci et al. 2011). However, this is not the only cause of weak emission lines, as discussed more fully in Cooper et al. (2013). In particular, there is no real evidence for underlying absorption in the Br $\gamma$  line as is often seen in weakly accreting T Tauri stars.

Figure 5 presents the Br $\gamma$  emission line images. They have a similar appearance to the continuum images. In AFGL 2136, the V-shaped feature is not detected because of the low SNR. The nebulosities are somewhat extended with the typical FWHM sizes of 0.2 arcsec apart from I19065 and V645 Cyg, in which the values are 0.13 arcsec and 0.1 arcsec, respectively. These extensions are the same as those of the nearby continuum. These results suggest that the Br $\gamma$  emitting region is so compact and close to the central star that they are not resolved with an 8 m single aperture telescope and the nebulous features seen in the images are light scattered by the circumstellar dusty envelope or disc. This was also concluded for the MYSO W33A (D10).

We performed three-dimensional spectro-astrometry to analyse the small-scale geometry of the Br $\gamma$  emission. Spectro-astrometry is a technique that measures the positional centroid of the emission at an accuracy exceeding the diffraction limit, see e.g. Baines et al. (2006). D10 successfully revealed a signature of a bipolar jet in the Br $\gamma$  emission line with a sub-mas position offset between the blueshifted and redshifted components. We consider velocity ranges between  $-800 \text{ km s}^{-1}$  and  $+400 \text{ km s}^{-1}$  for V645 Cyg and be-



**Figure 5.** The Br $\gamma$  images. The orientation of the images are the same as Fig. 2.



**Figure 6.** Spectro-astrometry across the Br $\gamma$  emission line. The coloured dots indicate the measured centroid positions at individual velocity channels. The velocity ranges are between  $-800 \text{ km s}^{-1}$  (indicated with blue) and  $+400 \text{ km s}^{-1}$  (indicated with red) for V645 Cyg and between  $\pm v_{\text{FWZI}}$  for other objects. The zero-point indicates the position centroid of the nearby continuum.



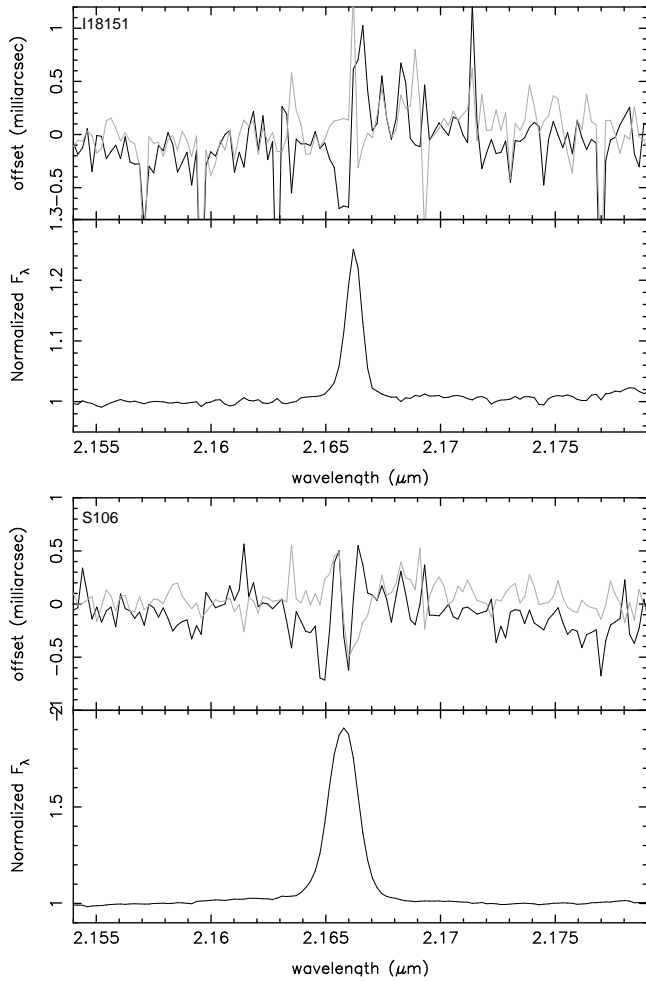


**Figure 7.** Spectro-astrometry of the Br $\gamma$  emission line for I18151 (top panel) and S106 (bottom panel). The black and grey lines are for the right ascension and declination, respectively.

tween  $\pm v_{FWZI}$  for other objects. In each velocity (wavelength) channel, the astrometric centroid was calculated. We also applied the same procedure to the telluric standard stars to estimate the accuracy of the position centroid and find 0.1 – 0.4 mas. Figure 6 presents the results of the spectro-astrometry for all of our sources across the Br $\gamma$  emission line. The positional offsets are shown with respect to the location of the continuum emission.

In most cases, the trails seem to show random walk like patterns. The random walk pattern as seen in I19065 covers a larger range than in the other such sources, and is especially pronounced near the systemic velocity. This is consistent with the classification of this object in the RMS database as a weak, and very compact, HII region. AFGL 2136 shows a strong excursion near the systemic velocity, which may also be evidence for a weak extended and, in this case, asymmetric HII region.

The strongest coherent features however are shown by I18151 and S106. Figure 7 shows the centroid positions of right ascension and declination of these objects, which are indicated with black and red lines, respectively. In both cases, the position centroids vary randomly at the nearby continuum, with an error of about 0.1mas, consistent with

the accuracy as measured on the telluric standard stars. However significant excursions can be seen across the line Br $\gamma$  line itself, consistent with an east-west signature in I18151 for example, as also shown in Fig. 6. Hence we conclude that the spectro-astrometry traces real effects across the emission line.

In S106, the highest velocity points are separated by  $\sim 0.4$  mas with a position angle of  $\sim 100^\circ$  east of north. This agrees reasonably well with the observed orientation of the radio emission at the core ( $\sim 119$  east of north) as shown by (Hoare et al. 1994). Both of these lie perpendicular to the orientation of the ionised bipolar lobes seen in images of the more general HII region around S106 (Hoare et al. 1994). Therefore our spectroastrometric signature is consistent with a source in the ionised gas in, or arising from, a circumstellar disc (including a possible disc-wind). The inner part of the bipolar lobes are themselves traced in the spectroastrometric data near systemic velocities by the large positional offsets across a range of angles centred on a NNE–SSW direction.

The offset of  $\sim 0.4$  mas between the blue and red components corresponds to 0.68 AU at 1.7 kpc. The velocity of the gas at these points is approximately  $\pm 200 \text{ km s}^{-1}$  around the systemic velocity. Assuming Keplerian rotation, and given the almost edge-on orientation of  $83^\circ$  (see Section 4.2.1), we estimate a central mass of  $\sim 22 \pm 5 M_\odot$  (where the error is solely that from the spectroastrometric accuracy). This is consistent with the inferred spectral type and luminosity as given in Table 2. It should be noted that the true separation between the blue and red components of the rotating material is likely to be larger than the aforementioned value. The contribution to the total flux from the line emission of the rotating material is smaller than that of the continuum and the stellar component for all our sources. The centroid of the total spectrum therefore lies nearer to the continuum than a “pure line” spectrum would be.

In I18151 a similar pattern is seen at high velocity, with a position angle of approximately  $90^\circ$ . A larger scale collimated jet detected in molecular hydrogen extends from southeast to northwest (D04). We see the southeast part of this jet clearly, as shown by Fig. 3. As noted previously however, it appears that the H $_2$  jet initially starts in a much more southerly direction within the inner 0.5 arcseconds, perpendicular to the spectroastrometric signature seen in Br $\gamma$ . We therefore again ascribe the source of the Br $\gamma$  emission to a circumstellar disc, or disc-wind.

The size of the disc is less clear from the data for I18151 than it is for S106. However, the same analysis as for S106, assuming an inclination angle of  $66^\circ$  (again see Section 4.2.1), gives a lower limit to the mass of  $\sim 10 \pm 5 M_\odot$ . This is again consistent with the known properties of this source.

## 4.2 CO $\nu = 2 - 0$ lines

### 4.2.1 Bandhead emission

In I18151, S106, and V645 Cyg, the CO  $J = 2 - 0$  bandhead emission is detected (as previously seen in S106 by Chandler et al. (1995) and in V645 Cyg, as discussed in Clarke et al. (2006)). Fig. 8 presents the spectra. S106 shows a clear double-peaked profile at the bandhead.

**Table 4.** The fitting results of the CO bandhead emission feature. The second line for each object indicates the range of parameter space searched over. The errors were calculated by holding all but one parameters constant at their best fitting value, and varying the selected parameter until the difference in  $\chi^2$  was equal to unity. The error of  $R_{\text{out}}$  is not presented because  $R_{\text{out}}$  is defined as the radius at which the temperature drops to 1000 K. Below this temperature, the  $\nu = 2 - 0$  emission is no longer excited. The error values indicated with an asterisk are not well determined because they lie at the boundary limit of the scanned ranges.

target	$R_{\text{in}}$ AU	$R_{\text{out}}$ AU	$i$ deg	$T_0$ K	$\Delta v$ kms $^{-1}$	$\log N_{\text{CO}}$ cm $^{-2}$	$\chi^2$
I18151	$2.4^{+5.8}_{-1.4}$	28.6	$79^{+11.3*}_{-49*}$	$4400^{+600*}_{-2250}$	$5.3^{+4.2}_{-5.2*}$	$21.4^{+5.4}_{-17}$	8.35
	0.37 – 8.0		30.0 – 90.0	1000 – 5000	0.1 – 50.0	1.0 – 50.0	
S106	$0.3^{+0.26}_{-0.11}$	4.0	$89.7^{+0.3*}_{-39*}$	$4600^{+400*}_{-1800}$	$1.2^{+5.3}_{-1.1*}$	$22.7^{+17*}_{-1.8}$	1.74
	0.1 – 5.8		50.0 – 90.0	1000 – 5000	0.1 – 50.0	4.0 – 50.0	
V645 Cyg	$3.2^{+0.7}_{-2.8*}$	44	$10.0^{+25}_{-10*}$	$4900^{+100*}_{-900}$	$46.6^{+29}_{-34.8}$	$20.0^{+0.7}_{-15}$	3.48
	0.1 – 5.0		0.0 – 50.0	1000 – 5000	0.1 – 100.0	1.0 – 50.0	

The interpretations of the spectral shape of the bandhead have been provided by several authors (Chandler et al. 1995; Najita et al. 1996; Kraus et al. 2000). Figure 2 in the paper by Najita et al. (1996) is instructive to explain the spectral features of a disc model. The emission of a single line from an inclined Keplerian rotating disc is described with the double-horned rotational broadening function. The model bandhead is then simply the convolution of this broadening function with the intrinsic CO emission. This leads to a distinct “blue shoulder” of the bandhead where there is blue shifted emission relative to the line of sight, which sets a constraint on both the line width and the inclination of the source. This is clearly seen in S106. It should be noted that a double-peaked feature can also be reproduced with a wind model (Chandler et al. 1995), when the opening angle of the conical wind is so small that the observer sees the red component only from the far side and the blue component only from the front side. This is not the case in S106 because this object is seen near to edge-on (Bally & Scoville 1982; Schneider et al. 2007; Saito et al. 2009).

The spectral features of V645 Cyg can also be explained with the same models. The emission peak is located around  $2.293 \mu\text{m}$ , which is between the blue shoulder and red peak in S106 and where the difference of the system velocities is negligible. In the face-on case, the rotational broadening function is single-peaked, and the peak stays at the bandhead wavelength. In this object, only the blueshifted components are detected in the [S II] and [O I] outflow emissions (Hamann & Persson 1989; Acke et al. 2005). This result indicates that the system is seen near face-on and the redshifted part is obscured by the equatorial material, presumably an accretion disc. A single-peak is also reproduced in a wind model if the opening angle of the wind is large. However we would then expect the peak of the emission to be shifted redwards compared to the nominal  $v_{\text{LSR}}$  of the source and it clearly is not.

For I18151, the data, although noisy, show no significant emission bluewards of the peak of the bandhead that cannot be explained by simple line broadening. The inclination angle of I18151 is estimated to be  $60^\circ$  (Fallscheer et al. 2011), intermediate between the cases of S106 and V645 Cyg, and

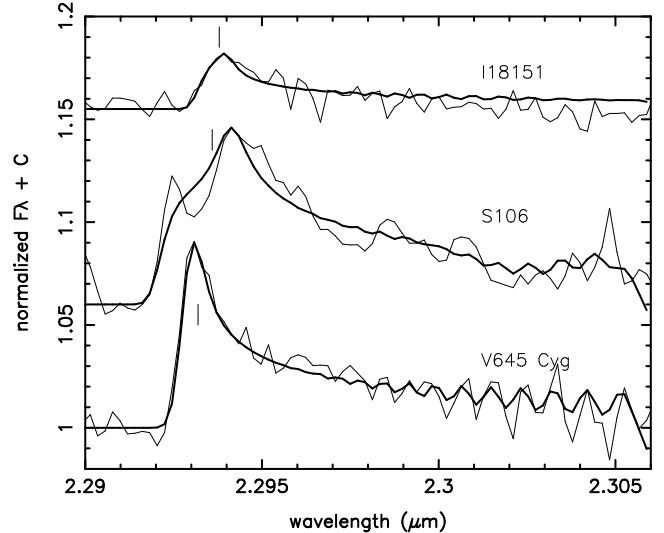


**Figure 8.** CO  $\nu=2-0$  bandhead spectra. The thin and thick lines denote the observations and the model results, respectively. The bars around  $\lambda = 2.293 \mu\text{m}$  indicate the local standard of rest.

the appearance of the spectrum is consistent with this if the origin of the emission is a disc.

We have also used a simple model of the gas phase CO disc to fit the data. We analyze the spectra attributed to the CO first over-tone bandhead emission based on Kraus et al. (2000) to derive the physical parameters of the disc geometry (see also Wheelwright et al. 2010; Ilee et al. 2012). In our model, up to  $J = 100$  rotational levels for the  $\nu = 2 - 0$  under the local thermodynamic equilibrium are considered. The CO energy levels are calculated with the  $Y_{k,l}$  parameters (see equation (6); Kraus et al. 2000; Farrenq et al. 1991), and the Einstein coefficients are taken from Chandra et al. (1996). The CO/H $_2$  ratio is assumed to be  $10^{-4}$ . For the disc geometry, we use a temperature gradient model,  $T(r) = T_0 (r/R_{\text{in}})^{-p}$ , and a geometrically thin disc with a surface density  $\Sigma(r) = \Sigma_0 (r/R_{\text{in}})^{-q}$ , where  $r$  is the distance from the central star. The disc has inner and outer radii of  $R_{\text{in}}$  and  $R_{\text{out}}$ , respectively, and is tilted with an inclination angle,  $i$ , where  $i = 0^\circ$  indicates face-on.

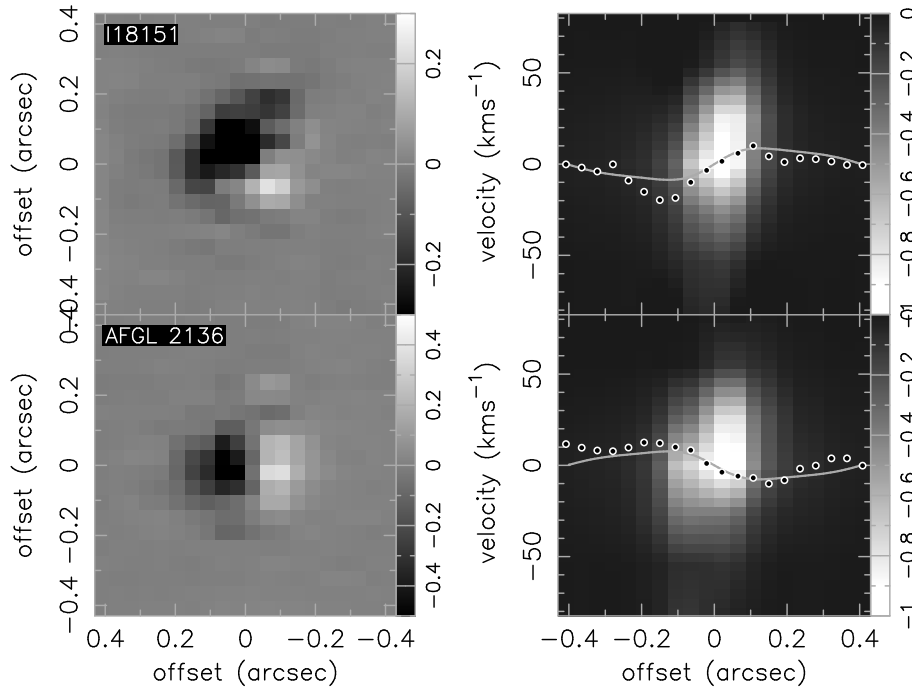


**Figure 9.** *Left:* the differential image between the blueshifted and redshifted components of the CO absorption features, i.e. the subtraction of the blue component flux image from the red one. *Right:* the position-velocity map at the inner  $20 \times 20$  pixel ( $0.86 \times 0.86$  arcsec) region. The top and bottom panels are the results of I18151 and AFGL 2136, respectively. The white circles are the velocity centroids of the observed data. The grey lines denote the Keplerian velocity plot convolved with Gaussian functions with the PSF sizes, where the central masses of  $30 M_{\odot}$  and  $20 M_{\odot}$  are assumed for I18151 and AFGL 2136, respectively.

The CO molecules are assumed to have a Keplerian rotating motion  $v_{\text{CO}} = \sqrt{GM_{\star}/r}$ , where  $G$  and  $M_{\star}$  are the gravitational constant and the stellar mass, respectively. The disc is divided into 75 radial rings each with 75 azimuthal cells. The intrinsic line shape of each transition has a Gaussian function with a line width of  $\Delta v$ . The total spectra are obtained by summing the flux from individual cells, in which the wavelength shift due to the rotational velocity of the disc is taken into account. The outer radius is set by the condition that the gas phase temperature drops below 1000 K, at which point the  $\nu = 2 - 0$  emission is no longer excited. In addition, the C-O bonding is dissociated at temperature above 5000 K. Hence, the maximum temperature is chosen not to exceed 5000 K. With these physical assumptions the CO bandhead spectra are produced and compared to the observed spectra using an IDL script. The best fit model parameters are found using  $\chi^2$  minimization. We examine the three objects with CO emission, I18151, S106 and V645 Cyg. The distance and the stellar mass are assumed to be 2.0 kpc and  $15 M_{\odot}$  for I18151, 1.7 kpc and  $20 M_{\odot}$  for S106, and 3.6 kpc and  $20 M_{\odot}$  for V645 Cyg (see Table 2). With these assumptions, we searched for the best fit parameters of  $R_{\text{in}}$ ,  $R_{\text{out}}$ ,  $p$ ,  $q$ ,  $i$ ,  $T_0$ ,  $\Delta v$ , and the column density of CO,  $N_{\text{CO}} (= \Sigma_{0,\text{CO}})$ . It turned out that the  $p$  and  $q$  parameters have particularly large uncertainties. Hence, we set fixed values of  $(-0.6, -1.5)$ , respectively, which are derived for intermediate mass stars (Ilee et al. 2012). The results of other six parameters are presented in Table 4. Only  $i$  and  $T_0$  are estimated with good accuracy. A similar analysis was done for S106 by Chandler et al. (1995). Although the estimated inclination angle they used of  $i = 65^\circ$  is somewhat

different from ours, their estimate of the size of the CO emitting region of 0.8 to 1.5 AU is in reasonable agreement. In both S106 and V645 Cyg, the best fitting inclination angle is consistent with the qualitative expectations discussed previously, as well as available results from the literature as given in Appendix A, suggesting that our estimated stellar masses are also reasonable.

#### 4.2.2 The low $J$ absorption transitions

D10 analysed the low  $J$  absorption line velocity structure of CO  $\nu = 2 - 0$ . Their data show a pair of blueshifted and redshifted components at east and west with respect to the flux peak position in the  $K$ -band continuum in W33A. They found the classical signature of a Keplerian rotating structure in the position-velocity (PV) diagram and a central mass of  $15 M_{\odot}$ , which includes the masses of the central star and the hot gas inside the cool gas region.

Both I18151 and AFGL 2136 show absorption features in the low  $J$  transition of CO  $\nu = 2 - 0$ . From the cube data, we used 11 absorption lines, which appear between  $2.32 \mu\text{m}$  and  $2.35 \mu\text{m}$  (Black & Willner 1984). We first derived the wavelength positions of individual absorption features, which are regarded as the zero-velocity. The images of all branches are aligned with the relative velocity and are added to increase the signal-to-noise ratio. Then, the differential images between the redshifted ( $v > 0$ ) and blueshifted ( $v < 0$ ) components, i.e. the subtraction of the blueshifted component image from the redshifted component images, the images of the velocity centroids, and the PV diagrams are made.

The top and bottom panels of Fig. 9 show the results of I18151 and AFGL 2136, respectively. The velocities range between  $\pm 15 (\pm 10)$   $\text{km s}^{-1}$  for I18151 and  $\pm 10 (\pm 7)$   $\text{km s}^{-1}$  for AFGL 2136. Although the standard deviations in velocity are large, we can clearly see a pair of redshifted and blueshifted components in the  $B - R$  images (left panels). The separations and the position angles of these components are obtained by measuring the absorption centroids of the blueshifted and redshifted components to be 0.038 arcsec at  $+31^\circ$  for I18151 and 0.054 arcsec at  $+91^\circ$  for AFGL 2136 with typical errors of one tenth of a pixel on the centroid and  $5^\circ$  on the angle. Applying a slit along these position angles, the PV diagrams are made (right panels) and the velocity centroid at each position pixel (0.043 arcsec spacing) is plotted with pink dots, with a typical error on the velocity of better than one tenth of a resolution element, or  $\text{km s}^{-1}$ . The redshifted component is located on the right side of the panel. In the velocity centroid maps, we see a skew, which is often seen in objects with Keplerian rotation, though the correspondence with a Keplerian model is not perfect even given the estimated errors. If we assume that this is also the case in our results, we can estimate the central masses. For this purpose, we made a simple model. The Keplerian rotating velocity of the CO gas,  $v_{\text{CO}}$ , is calculated by  $v_{\text{CO}} = \sqrt{GM/r}$ , where  $M$  is the central mass. The inclination angles,  $i$ , and the distances to these objects are assumed to be  $60^\circ$  and 2.0 kpc for I18151 (Fallscheer et al. 2011) and  $70^\circ$  and 2.0 kpc for AFGL 2136 (Kastner et al. 1992; Murakawa et al. 2008; de Wit et al. 2011). To allow direct comparison with the observations, the resulting velocity curve is obtained by convolving Gaussian functions with the PSF sizes (0.1 arcsec). In the PV diagram, the modeled velocity curves are plotted with green lines. The observed and model data are sufficiently similar to conclude that we do see Keplerian rotation in the cool absorbing gas in these sources. The resultant central masses are  $30 M_\odot$  for I18151 and  $20 M_\odot$  for AFGL 2136, with error of approximately 10% assuming the Keplerian model is a good fit.

The central mass of  $30 M_\odot$  for I18151 is larger than that of the inferred mass for a B0 star of  $15 M_\odot$  that was used in modelling the CO bandhead emission. However, the absorbing gas includes the mass of not only the central star but also all the gas located inside the maximum extent of the region of absorbing gas. Although the error on these measurements is large enough to suggest both absorption and emission kinematical masses could be equivalent, it may also suggest a larger reservoir of material still available for accretion by the central star. The large  $220 M_\odot$  mass found for the “disc-like” structure by Fallscheer et al. (2011) is certainly consistent with the picture in which more accretion could take place. A similar situation was found by D10 for W33A as well.

The orientation of the redshifted and blueshifted components in the CO  $\nu = 2 - 0$  absorption line is nearly northeast-southwest in I18151, perpendicular to the larger scale outflow. This is notably different from both the ionised spectroastrometric signature seen for  $\text{Br}\gamma$ , and the small scale north-south  $\text{H}_2$  jet we see in our data. It is possible that the outflow is precessing with time, though no intermediate angles are seen in the  $\text{H}_2$  jet by D04. It is also possible that the jet initially launches in a north-south direction, but is deflected by the larger scale molecular envelope in the

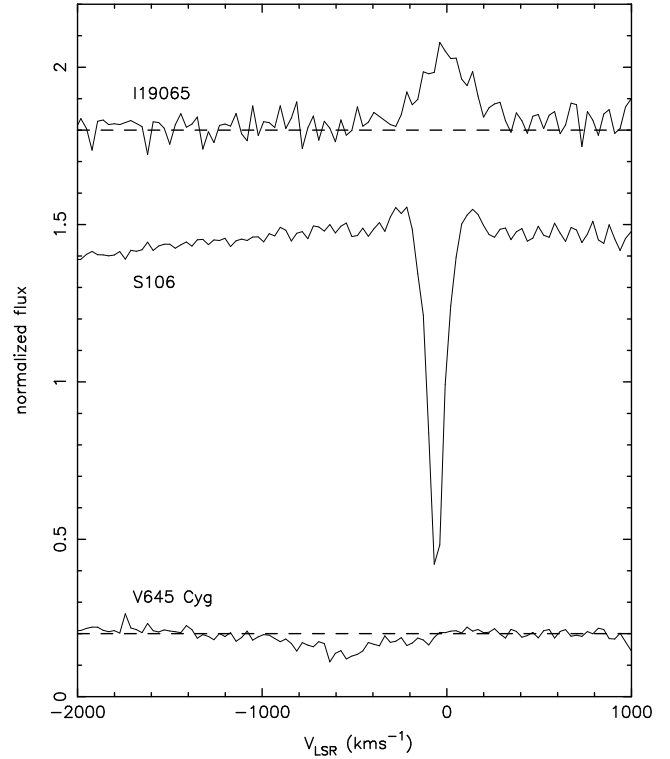


**Figure 10.** Spectral features of the He I at  $2.05689 \mu\text{m}$  on velocity scale.

observed southeast-northwest direction. In either case, the structure of the accreting gas in the immediate vicinity of the star appears to lie at different orientations when moving further away from the star.

The orientation of the CO absorption in AFGL 2136 is also puzzling. The blue- and red-shifted components of the absorption centroid lie at a position angle of  $90^\circ$  with a separation of  $\sim 100$  AU. As noted in Appendix A, the observed outflow axis runs SE–NW, consistent with the polarisation disc with a position angle of  $\sim 45^\circ$  found by Murakawa et al. (2008). It is possible that the distribution of mass on a few thousand AU is different from that on hundreds AU, i.e. a simple axisymmetric structure may not be applicable in this object, just as appears to be the case for I18151. Nevertheless, by assuming a Keplerian rotating motion in the cold CO gas, the velocity structure can be reproduced well with a  $20 M_\odot$  mass model. Although the stellar parameters of AFGL 2136 have not been precisely determined, it corresponds to a late O zero-age main sequence star in terms of the estimated luminosity of  $5.3 \times 10^4 L_\odot$ , corresponding to a  $20 - 25 M_\odot$  star.

#### 4.3 He I and other ionised and atomic emission lines

In our sample, the He I  $2^1P - 2^1S$  ( $\lambda = 2.05869 \mu\text{m}$ ) line is detected in I19065, S106, and V645 Cyg, and the  $4^{1,3}S - 3^{1,3}P$  ( $\lambda = 2.1128/2.1137 \mu\text{m}$ ) blend is present as a weak absorption feature in S106. Figure 10 presents the line profile on a  $v_{\text{LSR}}$  scale for the  $2^1P - 2^1S$  in all three objects. We see emission in I19065 and absorption in S106 and V645 Cyg. Notably the emission feature seen in I19065

is broader than expected from unresolved emission from the ionised HII region, suggesting that this, like the Br $\gamma$  emission, arises from the star in this source.

Clark & Steele (2000) have obtained *K*-band spectra of Be stars, and Hanson, Conti & Rieke (1996) and Hanson et al. (2005) of a more general sample of OB stars of all classes. The trends with spectral type are relatively clear and can be used to classify the emission as seen in our targets. HeI  $2^1P - 2^1S$  appears in emission in later type stars in dwarfs, giants and supergiants, and in many of the B0Ve and B1Ve stars in Clark & Steele (2000), and in Oe stars with types as early as O6Ve in Hanson, Conti & Rieke (1996). The lack of any detectable  $4^{1,3}S - 3^{1,3}P$  line in I19065 however suggests a relatively narrow range of type of around B0Ve or B1Ve, which is consistent with the known luminosity of this source from the RMS survey (Mottram et al. 2011).

Drew et al. (1993) previously detected the  $2^1P - 2^1S$  line in S106, mostly in absorption as we also see it. They argue that this absorption probably arises due to high optical depth in the 584 Å line and a high electron density ( $n_e \gtrsim 10^8 \text{ cm}^{-3}$ ). The FWHM is 65  $\text{km s}^{-1}$  and is in good agreement with the result of 70  $\text{km s}^{-1}$  by Drew et al. (1993). This velocity width is significantly smaller than that of the Br $\gamma$  emission lines ( $\sim 100 - 200 \text{ km s}^{-1}$ ). Drew et al. (1993) proposed that this line traces the region where the outflow from a disc-wind is still accelerating. Weak HeI  $4^{1,3}S - 3^{1,3}P$  absorption is seen, but there is no NIII 8-7 emission at  $\sim 2.116 \mu\text{m}$  emission as would be seen in earlier spectral types (Hanson, Conti & Rieke 1996). This suggests a type of O9Ve–B0Ve. We also carried out a spectroastrometric study of the  $2^1P - 2^1S$  line given its strength. Overall there is only a weak signature near the systemic velocity, in the direction of the bipolar nebula, perhaps consistent with a slight degree of infilling of the absorption line profile by larger scale nebular emission. Our lower resolution spectroscopy taken for the RMS survey (Cooper et al. 2013) shows nebular HeI  $2^1P - 2^1S$  emission consistent with this. The spectroastrometry does not show evidence for any other feature. In particular, there is nothing similar to the disc like structure seen in Fig. 6.

In V645 Cyg, the absorption feature is strongly blueshifted and appears around  $v \sim -800 \text{ km s}^{-1}$ . A similar trend is seen in the spectrum presented by Clarke et al. (2006). However, the spectral feature spreads up to  $-2000 \text{ km s}^{-1}$  in their data, but is detected only up to  $-1000 \text{ km s}^{-1}$  in our spectrum. V645 Cyg changes its spectral appearance regularly, complicating any attempts to derive an exact spectral type. However, the spectra we have is consistent with approximately O9Ve, similar to S106. The star cannot be hotter, given the lack of NIII, and the lack of any HeI  $4^{1,3}S - 3^{1,3}P$  suggests it cannot be much cooler either.

The other metal lines that we see in our spectra, such as NaI, MgII or FeII are less sensitive to the spectral type. In all three cases it is plausible that the emission actually comes from the accretion disc rather than the stellar atmosphere (Lumsden et al. 2012).

Overall the HeI and other metal lines suggest a common picture in which a stellar wind or disc wind can be present, along with an accretion disc. It would be interesting to determine whether spectroastrometry could be used on some

of these metal lines in future higher signal-to-noise studies to test whether this scenario is correct.

## 5 CONCLUSIONS

We presented high-resolution *K*-band integrated field spectroscopy of six MYSOs obtained using the AO assisted NIFS instrument on the Gemini-north telescope. This observing technique allows us to analyse three-dimensional spectroscopy across emission and absorption lines. In the previous paper (D10), we successfully detected a bipolar jet like feature in the Br $\gamma$  emission line and a Keplerian rotating motion of the neutral CO gas disc around a  $\sim 15 M_\odot$  mass central star in W33A. In this new work, we increase the sample, with four out of six being already well studied and two new. Our new data display a number of spectral lines such as Br $\gamma$  emission lines, CO bandhead emissions and absorptions,  $\text{H}_2 \nu = 1 - 0 \text{ S}(1), \text{S}(2)$ , and HeI. Some clear features can be inferred from our data despite the heterogeneous nature of the sample.

All of our targets show evidence of Br $\gamma$  emission. The measured  $v_{\text{FWHM}}$  ranges between 100 and 200  $\text{km s}^{-1}$ , which is consistent with stellar wind or disc-wind velocities (Bunn et al. 1995). In V645 Cyg, the P-Cygni profile is detected in a velocity range between  $-800 \text{ km s}^{-1}$  and  $-300 \text{ km s}^{-1}$ . This is consistent with a spherical wind. In the Br $\gamma$  emission images, the appearance is similar to those of the *K*-band continuum images in all objects, suggesting that these features are seen in scattering by dust in the circumstellar disc or envelope.

There is a clear spectroastrometric signature in both S106 and I18151, running perpendicular to the known larger scale outflow axis in both cases. At least for S106, the orientation is consistent with the disc-wind picture previously developed for this source, and we conclude the same should be true for I18151 as well. This is the opposite of what D10 saw in W33A, where the best explanation for the spectroastrometric signature was an ionised bipolar jet. In the two cases presented here it would suggest that the signature arises in ionised gas in, or from, a disc around the star. In the case of the well studied S106, the orientation of our spectroastrometric disc is also consistent with the morphology of the radio emission observed by Hoare et al. (1994). The presence of a stellar wind in this object is clear from the strong HeI absorption, lending support to the disc-wind picture of Drew et al. (1993). The estimates that are derived for the stellar masses from the spectroastrometry assuming Keplerian orbits, although clearly imprecise due to the scatter in the data as shown in Fig. 6, and strictly lower limits, are consistent with the known properties of these sources. The evidence that these two sources contain discs is therefore strong.

The other objects show spectroastrometric data consistent with a null result in most cases, revealing only a random-walk like pattern, though AFGL 2136 may show evidence for a weak HII region near the systemic velocity. I19065 shows a larger scatter in its random-walk pattern than the other non-detections. This may be due to “contamination” of the stellar spectrum due to the extended nebular HII region emission. The lack of any signature in V645 Cyg, given the excellent signal-to-noise for that source, places a

strong constraint on what we see there, consistent with the P-Cygni wind profile observed in the line.

Evidence for a disc from CO bandhead emission was present in I18151, S106 and V645 Cyg. The disc parameters for I18151 and S106 are consistent with those found from our analysis of the spectroastrometry of Br $\gamma$ . The edge-on nature of S106 is clearly seen in these data as well. V645 Cyg shows evidence for a more pole-on orientation, which may be why we see no evidence for a disc-wind component in this source in the spectroastrometry. It may also simply be that V645 Cyg is relatively more evolved than the other sources.

Finally, in I18151 and AFGL 2136, a series of CO absorption lines are detected. If we assume that these lines originate from the CO gas disc and the velocity structures reflect the Keplerian rotating motion, the central masses can be estimated. Our data show a separation of the flux centroids between the blueshifted and redshifted components. This orientation is nearly perpendicular to the jet direction in I18151, giving a strong evidence for a rotating motion in our data, whereas that orientation is less correlated with the direction of the outflow or the NIR polarization disc in AFGL 2136. Nevertheless, the rotation velocities and the central masses are estimated to be  $\pm 15(\pm 10)$  km s $^{-1}$  and  $30 M_{\odot}$  for I18151 and  $\pm 10(\pm 7)$  km s $^{-1}$   $20 M_{\odot}$  for AFGL 2136.

Our work has demonstrated that three-dimensional spectroastrometry across spectral emission and absorption lines is a powerful diagnostic technique to study the geometrical and kinematic properties of ionized or molecular regions in vicinity of the central star. The ionized hydrogen traces the mass accretion channel inside the accretion disc and disc winds, which is driven by the central star. On the other hand, the molecular gas probes the Keplerian rotating discs. The consistency of the results obtained using different methods strongly supports the hypothesis that massive stars form by mass accretion via circumstellar discs.

## ACKNOWLEDGMENTS

Based on observations (proposal ID: GN-2011A-Q-56) obtained at the Gemini Observatory, which is operated by the Association of Universities for Research in Astronomy, Inc., under a cooperative agreement with the NSF on behalf of the Gemini partnership: the National Science Foundation (United States), the Science and Technology Facilities Council (United Kingdom), the National Research Council (Canada), CONICYT (Chile), the Australian Research Council (Australia), Ministério da Ciência, Tecnologia e Inovação (Brazil) and Ministerio de Ciencia, Tecnología e Innovación Productiva (Argentina). We thank the referee, Dr. Scott Wolk, for his helpful comments.

## APPENDIX A: PROPERTIES OF INDIVIDUAL OBJECTS

### A1 I18151

I18151 ( $D = 3$  kpc) has been studied well, having featured in a large number of survey observations of MYSO candidates (Sridharan et al. 2002; Beuther et al. 2002). Images at the MSX 8  $\mu$ m (Marseille et al. 2008) and 1.2 mm

continuum (Beuther et al. 2002) wavelengths revealed four clumps MM1–4 spreading across  $\sim 1'$  scale. IRS 1 is located at MM1, which we observed. Fallscheer et al. (2011) performed a radiative transfer modeling of the dust disc of this object and obtained a luminosity of  $\sim 16000 L_{\odot}$ . However, the spectral energy distribution was not well constrained in the far infrared in their model. Unpublished Herschel PACS data at 70  $\mu$ m reveals a source with flux  $\sim 765$  Jy. Fallscheer et al. (2011) scaled all “large beam” flux down by a factor of four to match their mm interferometry. If we adopt the same correction, their best fit spectral energy distribution lies a factor of  $\sim 1.7$  too low. The Herschel data is only about 10% smaller than the published large beam IRAS flux we used to derive a luminosity of  $22000 L_{\odot}$  for the RMS database. It seems likely the luminosity is actually  $\sim 20000 L_{\odot}$  given these remarks, corresponding to a  $15 M_{\odot}$  star (Fallscheer et al. 2011). Fallscheer et al. (2011) also found a huge disc of  $220 M_{\odot}$  mass and 5000 AU radius from the mm interferometry. Only the inner 30 AU satisfy the Toomre criterion, a condition of gravitational stability (Toomre 1964). Hence, most of the mass of their modeled disc would include the outer envelope.

Our results are consistent with the luminosity and mass for the central star implied by these earlier results. The disc orientation we find in Br $\gamma$  is east-west, whereas the large scale H $_2$  jet traced by D04 lies NW–SE. The CO absorption agrees with the latter orientation. This suggests that the inner disc lies at an angle to the larger scale envelope structure.

### A2 AFGL 2136

Although a couple of stars or cores are often found in a high-mass star formation region, there is no other source within  $5'$  from AFGL 2136 in the mid-infrared and submillimeter wavelength ranges (Urquhart et al. 2009). The near-infrared images show three features with extensions of a few arcsec and the central proto-star is located at IRS 1 (Kastner et al. 1992). The CO emission line observations show a bipolar outflow extending at a position angle of  $\sim 135^{\circ}$  and the SE and NW components are blueshifted (14 to 20 km s $^{-1}$ ) and redshifted (24 to 30 km s $^{-1}$ ) respectively. The orientation of the polarization disc in the NIR data is found to be  $\sim 45^{\circ}$ , approximately perpendicular to the CO outflow direction (Minchin et al. 1991; Murakawa et al. 2008). These results indicate that the orientation of the equatorial plane lies at a position angle of  $\sim 45^{\circ}$ . The results of radiative transfer modeling suggest that the viewing angle is about  $70^{\circ}$ , i.e. seen near edge-on (Murakawa et al. 2008; de Wit et al. 2011). de Wit et al. (2011) found that a situation requiring both a gaseous disc and dusty envelope is needed to explain the observed mid-infrared interferometry. The observed baseline for their data lay along the position angle of the polarization disk.

Menten & van der Tak (2004) detected both water and class II methanol maser spots about 1 arcsec west with respect to IRS 1. These masers are usually tracers of outflows, but they do not align with the CO outflow presented by Kastner et al. (1992). Instead they lie perpendicular to the plane of the CO absorption feature we find. The strongest water maser feature found by Menten & van der Tak (2004) is redshifted with respect to the systemic velocity. Our

more recent water maser observations using the GBT (Urquhart et al. 2011) shows that this feature has weakened considerably, with the strongest component now arising much closer to the systemic velocity.

Menten & van der Tak (2004) concluded that this may be an example where the water maser arises in the infalling gas, in the post-shock gas just behind the accretion shock. It may be that the CO absorption disc is evidence for larger accretion flow that is “twisted” relative to the small scale gaseous disk suggest by de Wit et al. (2011), giving rise to a stronger shock than would otherwise be the case, and reconciling the position angles of the small scale disc and larger scale absorbing gas. Further observations are clearly required to fully resolve this puzzle.

### A3 S106

The inner circumstellar region of S106 has been studied by several authors (e.g. Bally & Scoville 1982; Hoare et al. 1994; Chandler et al. 1995; Ghosh et al. 2003; Schneider et al. 2007; Saito et al. 2009). The dark lane is thought to be an edge-on massive disc (Bally & Scoville 1982). Lucas et al. (1978) found a rotation axis of  $\sim 30^\circ$ , which is perpendicular to the dark lane. The radio spectrum at 22 GHz shows a flux,  $S_\nu$ , proportional to  $\nu^{0.7}$ , suggesting an ionized stellar wind (Panagi & Felli 1975). The wind has a high-mass loss rate of  $10^{-5} M_\odot \text{yr}^{-1}$  (Hippelein & Muench 1981; Felli et al. 1984). This is too high for OB type main sequence stars, indicating a young stellar object. The disc plane is well defined by the radio observations of Hoare et al. (1994) to be  $\sim 120^\circ$ .

Line observations have shown strong P-Cygni profiles in hydrogen recombination and He I (Drew et al. 1993) and double peaks in Br 12 and Fe II (Lumsden et al. 2012). These features can not be explained with an accretion flow, but suggest emission from stellar/disc winds or an accelerating outflow. This can be seen as consistent with the fact that the radio emission lies in the disc plane and not perpendicular to it if the source of both is a disc-wind type geometry (Hoare et al. 1994). Our own Br  $\gamma$  spectroastrometry is consistent with these previous findings, and the inferred stellar mass agrees with the observed luminosity.

### A4 V645 Cyg

The physical properties of the central star of V645 Cyg has been frequently studied since its identification (Lebofsky et al. 1976). It has a luminosity of about  $4 \times 10^4 L_\odot$  (Mottram et al. 2011). The near-infrared imaging polarimetry shows a centro-symmetric pattern surrounding N0 nebula (Minchin et al. 1991). Some H<sub>2</sub>O maser spots are detected exactly toward the N0 (Lada et al. 1981). The spectral type of the central star was estimated to be O7e (Cohen et al. 1977). On the other hand, Goodrich (1986) and Hamann & Persson (1989) detected the P-Cygni profiles in He I, O I, Si II, and Ca II, suggesting Herbig Ae/Be stars. Recently, Miroshnichenko et al. (2009) assessed the effective temperature from the optical spectroscopy. They suggest that  $T_{\text{eff}}$  is about 25000 K, but that the star is probably extended. Given the variability in the spectrum, it is not inconceivable that this result is in agreement with

the earlier result of Clarke et al. (2006), who found a temperature nearer 30000K, and a type near O9Ve as we do here (which is also more consistent with the known luminosity). The lack of He II emission as clearly pointed out by Miroshnichenko et al. (2009) is not a problem with this classification.

The P-Cygni profile is detected in Br  $\gamma$  (this work and Clarke et al. 2006). The blueshifted absorption component ranges up to  $-800 \text{ km s}^{-1}$  (cf.  $-2000 \text{ km s}^{-1}$ , Clarke et al. 2006). A similar profile is detected in W33A (D10). Our spectroastrometry of Br  $\gamma$  shows no significant signal. We suggest that this is due to the fact that Br  $\gamma$  arises in a spherically outflowing wind in this source, which essentially has a null spectroastrometric signature. This also naturally explains the strong P-Cygni profile. We previously concluded that W33A has an asymmetric wind by comparison. This suggests that V645 Cyg is actually nearer to its final main sequence configuration. Our fit to the CO bandhead also suggests that V645 Cyg must be close to pole-on.

### A5 I19065 and G082

These objects are identified as MYSOs by the RMS survey (Lumsden et al. 2002) and this work for the first time reports their individual study. I19065 is a weak HII region, with a small cluster of stars. The brightest of those seen at  $K$  may be the most important ionizing source. In I19065, the He I line at  $2.058 \mu\text{m}$  is detected in emission, as is Br  $\gamma$ . The width of the lines suggest an origin partly from the star as well as the HII region. The estimated bolometric luminosity is  $1.3 \times 10^4 L_\odot$  (Mottram et al. 2011). We find good agreement between this luminosity and a possible B1Ve classification from the properties of the He I  $2.058 \mu\text{m}$  line. G082 has no special characteristic besides the detections of the Br  $\gamma$  and Fe II emission lines in our data. Taking into account the estimated bolometric luminosity of  $6.3 \times 10^3 L_\odot$ , this object is probably a mid-B star.

## REFERENCES

- Acke, B., van den Ancker, M. E., & Dullemond, C. P. 2005, *A & A*, 436, 209
- Antoniucci, S., García López, R., Nisini, B., et al. 2011, *A & A*, 534, A32
- Bally, J. & Scoville, N. Z. 1982, *ApJ*, 255, 497
- Baines, D., Oudmaijer, R. D., Porter, J. M., Pozzo, M. 2006, *MNRAS*, 367, 737
- Beuther, H., Schilke, P., Menten, K. M., Motte, F., Sridharan, T. K., & Wyrowski, F. 2002, *ApJ*, 566, 945
- Bik, A., & Thi, W. F. 2004, *A & A*, 427, 13
- Black, J. H., & Willner, S. P. 1984, *ApJ*, 279, 673
- Bonnell, I.A., Vine, S.G., Bate, M.R., 2004, *MNRAS*, 349, 735
- Bunn, J. C., Hoare, M. G., & Drew, J. E. 1995, *MNRAS*, 272, 346
- Carr, J. S. 1989, *ApJ*, 345, 522
- Chandler, C. J., Carlstrom, J. E., & Scoville, N. Z. 1995, *ApJ*, 446, 793
- Chandra S., Maheshwari V. U., Sharma A. K., 1996, *A & AS*, 117, 557
- Clark, J. S. & Steele, I. A. 2000, *A & AS*, 141, 65

- Clarke, A. J., Lumsden, S. L., Oudmaijer, R. D., Busfield, A. L., Hoare, M. G., Moore, T. J. T., Sheret, T. L., Urquhart, J. S. 2006, *A&A*, 457, 183
- Cohen, M. 1977, *ApJ*, 215, 533
- Cooper, H.D.B., Lumsden, S.L., Oudmaijer, R.D., Hoare, M.G., Clarke, A.J., Urquhart, J.S., Mottram, J.C., Moore, T.J.T., Davies, B., 2013, *MNRAS*, 430, 1125
- Corcoran, M. & Ray, T. P. 1998, *A&A*, 331, 147
- Davies, B., Lumsden, S. L., Hoare, M. G., Oudmaijer, R. D., & Willem-Jan de Wit, 2010, *MNRAS*, 402, 1504
- Davis, C. J., Varricatt, W. P., Todd, S. P., Ramsay Howat, S. K. 2004, *A&A*, 425, 981
- de Wit, W. J., Hoare, M. G., Oudmaijer, R. D., Nürnberger, D. E. A., Wheelwright, H. E., & Lumsden, S. L. 2011, *A&A*, 526, L5
- Drew, J. E., Bunn, J. C., & Hoare, M. G. 1993, *MNRAS*, 265, 12
- Drew, Janet E., Proga, D., & Stone, J. M. 1998, *MNRAS*, 296, L6
- Farrenq R., Guelachvili G., Sauval A. J., Grevesse N., Farmer C. B., 1991, *J. Molecular Spectrosc.*, 149, 375
- Fallscheer, C., Beuther, H., Sauter, J., Wolf, S., & Zhang, Q. 2011, *ApJ*, 729, 66
- Felli, M., Massi, M., Staude, H. J., Reddmann, T., Eiroa, C., Hefele, H., Neckel, T., & Panagia, N. 1984, *A&A*, 135, 261
- Folha, D. F. M., & Emerson, J. P. 2001, *A&A*, 365, 90
- Gehrz, R. D., Grasdalen, G. L., Castelaz, M., Gullixson, C., Mozurkewich, D., & Hackwell, J. A. 1982, *ApJ*, 254, 550
- Ghosh, S. K., Kulkarni, V. K., Ojha, D. K., & Verma, R. P. 2003, *BASI*, 31, 391
- Goodrich, R. W. 1986, *ApJ*, 311, 882
- Goto, M., Carmona, A., Linz, H., Stecklum, B., Henning, Th., Meeus, G., Usuda, T. 2012, *ApJ*, 748, 6
- Greene, T. P. & Lada, C. J. 1996, *AJ*, 112, 2184
- Hanson, M. M., Conti, P. S., & Rieke, M. J. 1996, *ApJS*, 107, 281
- Hanson, M. M., Kudritzki, R.-P., Kenworthy, M. A., Puls, J., & Tokunaga, A. T. 2005, *ApJS*, 161, 154
- Hamann, F., & Persson, S. E. 1989, *ApJ*, 339, 1078
- Hoare, M. G., Drew, J. E., Muxlow, T. B., & Davis, R. J. 1994, *ApJ*, 421, L51
- Hippelein, H. & Muench, G. 1981, *A&A*, 99, 248
- Ilee, J. D., Wheelwright, H. E., Oudmaijer, R. D., de Wit, W. J., Maud, L. T., Hoare, M. G., Lumsden, S. L., Moore, T. J. T., Urquhart, J. S., Mottram, J. C. 2012, *MNRAS*, accepted.
- Ishii, M., Nagata, T., Sato, S., Yao, Y., Jiang, Z., & Nakaya, H. 2001, *AJ*, 121, 3191
- Kastner, J. H., Weintraub, D. A., & Aspin, C. 1992, *ApJ*, 389, 357
- Kastner, J. H., Weintraub, D. A., Snell, R. L., Sandell, G., Aspin, C., Hughes, D. H., & Baas, F. 1994, *ApJ*, 425, 695
- Kahn F.D., 1974, *A&A*, 37, 149
- Kraus, M., Krügel, E., Thum, C., & Geballe, T. R. 2000, *A&A*, 362, 158
- Kraus S., et al., 2010, *Nature*, 466, 339
- Krumholz, M. R., Klein, R. I., McKee, C. F., Offner, S. S. R., Cunningham, A. J. 2009, *science*, 323, 754
- Kuiper, R., Klahr, H., Beuther, H., & Henning, T. 2010, *ApJ*, 722, 1556
- Kuiper, R., Yorke, H.W., 2013, *ApJ*, 763, 104
- Kurosawa, R., Romanova, M. M., & Harries, T. J. 2011, *MNRAS*, 416, 2623
- Lada, C. J., Blitz, L., Reid, M. J., & Moran, J. M. 1981, *ApJ*, 243, 769
- Lebofsky, M. J., Kleinmann, S. G., Rieke, G. H., & Low, F. J. 1976, *ApJ*, 206, L157
- Lucas, R., Encrenaz, P. J., Le Squeren, A. M., Kazes, I. 1978, *A&A*, 66, 155
- Lumsden, S. L., Hoare, M. G., Oudmaijer, R. D., Richards, D. 2002, *MNRAS*, 336, 621
- Lumsden, S. L., Wheelwright, H. E., Hoare, M. G., Oudmaijer, R. D., & Drew, J. E. 2012, *MNRAS*, 424, 1088
- Lumsden, S.L., Hoare, M.G., Urquhart, J.S., Oudmaijer, R.D., Davies, B., Mottram, J.C., Cooper, H.D.B., Moore, T.J.T., 2013, *ApJS*, submitted
- Marseille, M., Bontemps, S., Herpin, F., van der Tak, F. F. S., & Purcell, C. R. 2008, *A&A*, 488, 579
- Martin, S. C. 1997, *ApJ*, 478, L33
- McGregor, P. J., Hart, J., Conroy, Peter G. et al. in Iye M., Moorwood A. F. M., eds, *Proc. SPIE Conf. Ser. Vol. 4841, Instrument Design and Performance for Optical/Infrared Ground Tested Telescopes*. SPIE, Bellingham, 4841, 1581
- McKee, C.F., Tan, J.C., 2003, *ApJ*, 585, 850
- Mendigutía, I., Calvet, N., Montesinos, B., et al. 2011, *A&A*, 535, A99
- Menten, K. M. & van der Tak, F. F. S. 2004, *A&A*, 414, 289
- Miroshnichenko, A. S., Hofmann, K.-H., Schertl, D., et al. 2009, *A & A*, 498, 115
- Minchin, N. R., Hough, J. H., Burton, M. G., & Yamashita, T. 1991, *MNRAS*, 251, 522
- Mottram, J. C., Hoare, M. G., Urquhart, J. S., et al. 2011, *A&A*, 525, A149
- Murakawa, K., Preibisch, T., Kraus, S., Weigelt, G. 2008, *A&A*, 490, 673
- Muzerolle, J., Calvet, N., & Hartmann, L. 1998, *ApJ*, 492, 743
- Najita, J., Carr, J. S., Glassgold, A. E., Shu, F. H., & Tokunaga, A. T. 1996, *ApJ*, 462, 919
- Nisini, B., Milillo, A., Saraceno, P., Vitali, F. 1995, *A&A*, 302, 169
- Panagia, N. & Felli, M. 1975, *A&A*, 39, 1
- Persson, S. E., Geballe, T. R., McGregor, P. J., Edwards, S., Lonsdale, C. J. 1984, *ApJ*, 286, 289
- Richer, J. S., Padman, R., Ward-Thompson, D., Hills, R. E., & Harris, A. I. 1993, *MNRAS*, 262, 83
- Saito, H., Tamura, M., Kandori, R., et al. 2009, *AJ*, 137, 3149
- Schneider, N., Simon, R., Bontemps, S., Comern, F., & Motte, F. 2007, *A&A*, 474, 873
- Sharpless, S. 1959, *ApJS*, 4, 257
- Shu, F. H., Adams, F. C., & Lizano, S. 1987, *ARA&A*, 25, 23
- Sibille, F., Bergeat, J., Lunel, M., & Kandel, R. 1975, *A&A*, 40, 441
- Sridharan, T. K., Beuther, H., Schilke, P., Menten, K. M., & Wyrowski, F. 2002, *ApJ*, 566, 931
- Stecklum, B., Garatti, A. Caratti o, & Linz, H. 2012, *arXiv*, 1205, 2185
- Tokunaga, A. T. 2000, *Allen's Astrophysical Quantities*, 4th ed., ed. A. N. Cox (New York: AIP Press), 143



- Toomre, A. 1964, ApJ, 139, 1217
- Vacca, W. D., Cushing, M. C., & Rayner, J. T. 2003, PASP, 115, 389
- Urquhart, J. S., Busfield, A. L., Hoare, M. G., et al. 2007, A&A, 474, 891
- Urquhart, J. S., Hoare, M. G., Purcell, C. R., Lumsden, S. L., Oudmaijer, R. D., Moore, T. J. T., Busfield, A. L., Mottram, J. C., & Davies, B., 2009, A&A, 501, 539
- Urquhart, J. S., Morgan, L. K., Figura, C. C., Moore, T. J. T., Lumsden, S. L., Hoare, M. G., Oudmaijer, R. D., Mottram, J. C., Davies, B., Dunham, M. K., 2011, MNRAS, 418, 1689
- Wheelwright, H. E., Oudmaijer, R. D., de Wit, W. J., Hoare, M. G., Lumsden, S. L., & Urquhart, J. S. 2010, MNRAS, 408, 1840
- Yorke, H.W. & Sonnhalter, C., 2002, ApJ, 569, 846
- Zinnecker, H. & Yorke, H. W. 2007, ARA&A, 45, 481